# Understanding Shock Dynamics in the Inner Heliosphere with Modeling and Type II Radio Data: the 2010-04-03 event

H. Xie,[1] D. Odstrcil,[2] L. Mays,[3] O. C. St. Cyr,[4] N. Gopalswamy,[4] and H.

Cremades[5]

---

[1]Department of Physics, The Catholic

University of America, Washington DC,

USA.

[2]Department of Computational and Data

Sciences,George Mason University, Fairfax,

Virginia, USA.

[3]NASA Postdoctoral Fellow, Goddard

Space Flight Center, Greenbelt, Maryland,

USA

[4]Code 670, NASA/Goddard Space Flight

Center,Greenbelt, Maryland, USA.

[5]UTN-FRM/CONICET, Mendoza,

Argentina.

**Abstract.**    The 2010 April 03 solar event was studied using observations from STEREO SECCHI, SOHO LASCO, and Wind kilometric Type II data (kmTII) combined with WSA-Cone-ENLIL model simulations performed at the Community Coordinated Modeling Center (CCMC). In particular, we identified the origin of the coronal mass ejection (CME) using STEREO EUVI and SOHO EIT images. A flux-rope model was fit to the SECCHI A and B, and LASCO images to determine the CME's direction, size, and actual speed. J-maps from STEREO COR2/HI-1/HI-2 and simulations from CCMC were used to study the formation and evolution of the shock in the inner helio-sphere. In addition, we also studied the time-distance profile of the shock prop-agation from kmTII radio burst observations. The J-maps together with in-situ data from the Wind spacecraft provided an opportunity to validate the simulation results and the kmTII prediction. Here we report on a compar-ison of two methods of predicting interplanetary shock arrival time: the ENLIL model and the kmTII method; and investigate whether or not using the ENLIL model density improves the kmTII prediction. We found that the ENLIL model predicted the kinematics of shock evolution well. The shock arrival times (SAT) and linear-fit shock velocities in the ENLIL model agreed well with those mea-surements in the J-maps along both the CME leading edge and the Sun-Earth line. The ENLIL model also reproduced most of the large scale structures of the shock propagation and gave the SAT prediction at Earth with an er-ror of $\sim 1 \pm 7$ *hours.* The kmTII method predicted the SAT at Earth with an error of $\sim 15$ hours when using $n_0 = 4.16$ cm$^{-3}$, the ENLIL model plasma

27  density near Earth; but it improved to $\sim$2 hours when using $n_0 = 6.64$ cm$^{-3}$,

28  the model density near the CME leading edge at 1 AU.

## 1. Introduction

For decades groundbased telescopes have detected the slowly-drifting (downward in frequency) solar radio emissions at metric wavelengths called "Type II" radio bursts. When a shock travels outward from the solar corona, it accelerates electrons that in turn produce radio emission at the local plasma frequency ($f_p$ [kHz] $= 9 \sqrt{n_e}$ [cm$^{-3}$]) and its first harmonic ($2f_p$). As the shock encounters less-dense regions the local plasma frequency decreases giving rise to the slow-drift. These radio emissions can start at frequencies below 150 MHz in the low corona and extend down to the kilometric domain, slowly drifting to lower frequencies all the way to 1 AU, where the local plasma frequency of the solar wind is $\sim$25 kHz [*Gopalswamy et al.*, 2005a]. Since Earth's ionosphere blocks radio signals at frequencies below $\sim$10 MHz, the only way to detect the longer-wavelength emissions is by means of instruments in interplanetary space. These emissions have been regularly detected by the Wind Radio and Plasma Wave (WAVES) experiment [*Bougeret et al.*, 1995] and more recently by the Solar Terrestrial Relations Observatory (STEREO) WAVES [*Bougeret et al.*, 2008], whose space weather beacon makes them available in near-real-time.

Recently *Cremades et al.* [2007] described a novel technique to predict interplanetary (IP) shock arrival at L1 by measuring the drift rate of the kilometric ($\leq$300 kHz) Type II (kmTII) emissions. Shocks between 1997-2004 were identified from catalogues maintained by Wind and Advanced Composition Explorer (ACE) investigators, and altogether 160 kmTII radio bursts were identified in the Wind WAVES dataset. A subset of 84 kmTII events could be reliably measured and used to make a prediction as to when the shock

should be seen at L1. 66% of the predictions were within ±6 hours of the actual shock arrival time, and space weather forecasters have shown keen interest in incorporating this technique into their forecasts.

STEREO is comprised of two identical spacecraft orbiting the Sun ahead STEREO-A (STA) and behind STEREO-B (STB) Earth near the ecliptic plane [*Kaiser et al.*, 2008]. The two spacecraft separate away from Earth at a rate of about 22° per year. The extended solar minimum of 2007 - 2009 did not provide many earthward halo CMEs for the two STEREO spacecraft to study, but on April 3, 2010 a fast CME was observed to propagate towards Earth. The April 3 CME produced an interplanetary (IP) shock followed by an IP coronal mass ejection (ICME), which caused an extended geomagnetic storm with minimum Dst = -72 nT on April 5-7, 2010. During the storm, communication with the Galaxy 15 satellite was lost (W. Ferster, Intelsat Loses Contact with Galaxy 15 Satellite, Space News, 8 April 2010). Both STA [STB] observed the CME expanding off the West [East] limb around 09:00 UT; the Large Angle and Spectrometric Coronagraph Experiment (LASCO; *Brueckner et al.* [1995]) on board the Solar and Heliospheric Observatory (SOHO) observed the CME appearing as a halo event around 10:33 UT. The separation angles of STA [STB] with Earth were 67° [71°]. When we include SOHO, the three spacecraft (STA/B and SOHO) provided almost ∼ 140° view of the event. The Sun Earth Connection Coronal and Heliospheric Investigation (SECCHI) instrument package includes: the inner and outer coronagraph (COR1 and COR2), and the Heliospheric Imagers (HI1 and HI2)[*Eyles et al.*, 2009]. STEREO successfully tracked the April 3, 2010 event from the Sun into the heliosphere all the way to 1 AU. HI1 and HI2 image movies on STA showed clearly the evolution of the CME-driven shock in the heliosphere (see

online supplementary materials in the HTML). Furthermore, a kmTII radio burst was detected by Wind WAVES [*Bougeret et al.*, 1995] on April 4 from 00:58 until 16:33 UT. The associated shock arrived at the Wind spacecraft on April 5 07:48 UT. The wealth of data for this event provides us with a good opportunity to study the formation and the evolution of the CME-driven shock and to validate different methods of modeling and predicting IP shock dynamics and arrival time.

The April 3, 2010 event has been studied by several authors. *Möstl et al.* [2010] carried out an analysis of the in situ data of the associated IP shock and ICME that drove the shock. They showed that the ICME was a magnetic-cloud-like structure but it could not be fitted by any magnetic cloud models. By linking STEREO/SECCHI images to in situ observations, they demonstrated that the apex of the ICME was southward directed and only its northern flank passed over Earth. *Wood et al.* [2011] performed a thorough white-light analysis of the CME using an empirical flux-rope reconstruction and demonstrated that the CME could be fitted reasonably well with a 3D flux rope shape, where its orientation angle out of the ecliptic plane has been rotated from -80° (i.e., nearly N- S) close to the Sun to 10° (i.e., nearly E-W) far from the Sun. Using combined STEREO SECCHI imaging and the modeling of the CME driven shock, *Rouillard et al.* [2011] investigated the corresponding solar energetic particle (SEP) events measured at L1 and STB, and associated the origin and magnitude of the SEP event with the shock properties along different interplanetary magnetic field (IMF) lines.

In this paper, we perform a comprehensive study on the evolution and propagation of the April 3, 2010 CME/shock, combining STEREO and SOHO white light observations, kmTII radio data with the WSA-Cone-ENLIL model simulation. We use a flux rope model

[e.g. *Krall and St.Cyr*, 2006; *Xie et al.*, 2009] fit to SECCHI and LASCO observations to determine the CME speed, size and direction, as well as its time-distance profile when the CME is close to the Sun. To fully investigate the IP shock dynamics we use a heliospheric WSA-Cone-ENLIL simulation model. The fitted CME radial speed and half angular width are used to specify a hydrodynamic spherical cloud launched into the heliospheric computational domain. We derive the time-distance profile of the CME-driven shock in the heliosphere from J-maps (plots of elongation from the Sun versus time along fixed position angles [e.g., *Sheeley et al.*, 1999, 2008]) constructed from SECCHI images. The simulation results are directly compared with the SECCHI observations. We focus on two aspects in the paper: 1) using SECCHI and radio data to constrain the ENLIL model output; 2) determining whether or not a combination of techniques yields an improved prediction.

The paper is organized as follows: Section 2 presents the observations, including the CME solar source, flux rope model fit to coronagraphic images, and kinematic analysis with J-maps. Section 3 describes the WSA-Cone-ENLIL model simulation, and Section 4 gives the simulation results and comparison between the simulation results and obser- vations. Section 5 introduces the kmTII technique and applies the ENLIL model results to the method to improve the prediction. Finally, the discussion and conclusions are presented in Section 6.

## 2. Observations

### 2.1. CME Solar Source

The April 3, 2010 CME was an Earth-directed CME, which was associated with a X-ray flare with a peak flux level of B7.4 recorded by GOES X-ray monitor from NOAA Active

Region (AR) 11059 (S25W03) between 09:04 UT and 10:58 UT, with a peak at 09:54 UT. The flare was first seen in the Extreme Ultraviolet Imaging Telescope (EIT) on board SOHO between 09:14 UT and 10:00 UT with a faint EIT wave associated with the flare (http://cdaw.gsfc.nasa.gov/movie/make_javamovie.php?date=20100403&img1=soh_e195). The evolution of the flare showed a clear sigmoid to post-arcade structure, and the neutral line in the sigmoid active region was tilted ∼80° relative to the horizontal (east-west) direction (Figure 1b). On April 3, the separation angles of STA and STB with Earth are 67° and 71°, respectively. The flare was observed at S25E64 from STA and S25W74 from STB. An eruptive prominence (EP) was observed to the south of AR 11059 by SECCHI's Extreme Ultraviolet Imager (EUVI) at 304 $\overset{\circ}{A}$ on STA at 09:46 UT, as shown in Figure 1a. The prominence began to be active around 08:56 UT and erupted around 09:16 UT. EUVI 304 $\overset{\circ}{A}$ movie and EIT 195 $\overset{\circ}{A}$ movies show that both the prominence eruption and the X-ray flare eruption are related to the CME and the EP appeared as the CME core in COR1 around 10:15 UT. The flare location and post-eruption arcade are shown in Figure 1c as observed by EUVI 195 $\overset{\circ}{A}$ on STB at 11:00 UT.

## 2.2. CME Speed, Width and Propagation Direction: Flux Rope Model Fit

The CME was seen edge-on by COR1-A off the southeast limb starting at 09:05 UT, and by COR1-B off the southwest limb (http://cor1.gsfc.nasa.gov/catalog/). LASCO observed a halo CME on April 3 and its first appearance time in LASCO C2 was 10:33 UT. (http://cdaw.gsfc.nasa.gov/CME_list/). In Figure 2, we show the CME running difference images from STA/B COR1 and SOHO C2, respectively, along with the COR1(STA/B) and COR2-B original images at bottom panel. In COR2-B original image, a streamer ahead of the CME leading edge was clearly seen.

To determine the radial speed, angular width, and propagation direction of the CME, we applied a flux-rope model fit to SECCHI COR1 and COR2 and LASCO C2 and C3 images. The flux rope model used here is *Krall and St.Cyr* [2006]'s flux rope model (hereafter KS06). The KS06 model is also called the elliptical flux rope model, which assumes that the flux rope has an elliptical axis with varying radial circular cross-section. The coordinate system used in the KS06 model has its origin at the CME eruption region on Sun's surface, the $z$-axis directed towards North, the $x$-axis directed towards West, and the $y$-axis directed along the Earth-Sun line, away from Earth. *For simplicity,* the separation distance between two flux-rope footpoints has been neglected in the model. The geometry of the flux rope can be described by two parameters: the ratio of the semi-minor to semi-major axis of the ellipse $\lambda_\epsilon = R_2/R_1$ and the axial aspect ratio $\Lambda_\alpha = 2R_1/d$, where $R_1$, $R_2$ , and $d$ are semi-major axis, semi-minor axis and width of the flux rope at its apex [c.f. Figure 1 in *Xie et al.,* 2009]. The orientation of the flux rope is defined by three angles: latitude $\lambda$, longitude $\phi$, and tilt angle $\alpha$, where the tilt angle is the rotation around its central axis. We used an iterative method to parameterize the flux rope model. First, we chose initial test parameters of the flux rope model based on the coronagraphic observations; we then iteratively adjusted the test parameters until the best fit of the flux rope model to both SECCHI and LASCO images were obtained by visual examination.

Figure 3 shows the flux rope (FR) model fit for the CME; from left to right are COR1-A , C2 , and COR1-B images superimposed with the flux rope model projected wireframe (yellow curves) at t = 09:50 UT, 10:55 UT and 09:50 UT, respectively. The model best-fit radial distances to SECCHI COR1/2 and LASCO C2/3 image frames at different times yield the height-time profile of the CME (Figure 4), $R_{tip}(t)$, where $R_{tip}$ is the radial

162 distance from the origin to the apex of the FR. The widths of the CME are given by:

163 $\omega_{edge} = 2 \times tg^{-1}(0.5/\Lambda_\alpha), \omega_{broad} = 2 \times tg^{-1}(\lambda_\epsilon)$, where $\omega_{edge}$ and $\omega_{broad}$ are the widths of

164 the CME from edge-on and face-on views respectively. For the April 3 CME, the fitting

165 results gave that $R_1 = 0.8\ R_s$, $R_2 = 0.6\ R_s$, and $d = 2.0\ R_s$ at $R_{tip} = 2.6\ R_s$, where $R_s$

166 is the solar radius, which yielded $\omega_{broad} = 74°$ , and $\omega_{edge} = 64°$; the best-fit propagation

167 direction of the CME are $(\lambda, \phi, \alpha)$ = (-23°, 3°, -70°). Comparison of our fit direction

168 with previous studies shows that there is a very good agreement in longitude and decent

169 agreement in latitude and tilt angle. The CME direction determined in *Möstl et al.* [2010]

170 was S27° and W0°, and in *Wood et al.* [2011] was S16°, W2° with tilt angle of -80°.

171 Difference between *Wood et al.* (*Möstl et al.*)'s results and ours are 4° (7°), 3° (1°), 10°,

172 respectively, in $\lambda$, $\phi$, and $\alpha$.

173    Figure 4 shows the FR model fit height-time profile (solid line) and derived velocity

174 (dashed line) over-plotted with the GOES X-ray flux (blue dotted line). The velocities

175 are computed from adjacent data points of $R_{tip}$ and the uncertainties in the computed

176 velocity are estimated assuming the measurement uncertainty in distance $\pm\ 0.2\ R_s$ at 15

177 $R_s$ , i.e., the estimated fractional error in the distance is 1.3%. From the figure, we can see

178 that the April 3 CME is accelerated from 268 km/s to 873 km/s rapidly within the COR1

179 FOV and its velocity reached a small peak around 10:05 UT, which is roughly the peak

180 time of the X-ray flux, then accelerated gradually to 1011 km/s at $\sim$ 12:08 UT. Note,

181 however, that the resulting CME acceleration within the COR2 FOV should be taken

182 cautiously since the maximum velocity uncertainty is $\sim$ 150 km/s in the COR2 FOV,

183 which is almost half as large as the velocity variation. Comparison of our CME velocity

184 (1011 km/s) with those in *Möstl et al.* [2010] (990 km/s) and in *Wood et al.* [2011] (960

185  km/s) gives errors of 21 km/s and 51 km/s, respectively. These errors fall within the

186  maximum velocity uncertainty range.

### 2.3. Kinematic Analysis with J-maps

187  With the help of J-maps constructed from COR2, HI1 and HI2 images, we can derive

188  the CME trajectory in the heliosphere from near the Sun all the way to 1 AU [*Wood*

189  *et al.*, 2010]. Three methods have been generally used to infer radial distances, $r$, from

190  the measured elongation angles, $\epsilon$, from white light images: 1) Point-P [*Howard et al.*,

191  2006]; 2) Fixed-$\phi$ [*Kahler and Webb*, 2007; *Wood et al.*, 2010]; and 3) Harmonic Mean

192  [*Lugaz et al.*, 2009]. The Point-P method assumes a broad spherical front centered at the

193  Sun, and $r$ and $\epsilon$ are related by: $r = d \sin \epsilon$, where $d$ is the distance from the spacecraft to

194  the Sun. The Fixed-$\phi$ method assumes a very narrow CME traveling with fixed direction

195  with: $r = d \sin \epsilon / \sin(\epsilon + \phi)$, where $\phi$ is the angle between the CME trajectory and the line

196  of sight (LOS) from the observer to the Sun. The Harmonic Mean method approximates

197  the CME as a sphere centered halfway between the Sun and the CME's leading edge, and

198  yields a CME radial distance given by: $r = 2d \sin \epsilon / (1 + \sin(\epsilon + \phi))$, which is the harmonic

199  average of the Point-P and the Fixed-$\phi$ approximations.

200  We show in Figure 5, from left to right, running difference images of HI1-A ,HI2-A, and

201  a time-elongation J-map along the Sun-Earth line with PA $= 95°$, where PA is the position

202  angle measured counterclockwise from the north. Figure 5a shows three features of the

203  propagating CME: the southward ejecta (flux rope); the shock front with faint and sharp

204  brightness enhancements, extending much wider in latitude than ejecta; and the core at

205  rear of the flux rope. Note that there was a deformation at the shock front along the

206  CME central leading edge (LE; hereafter LE denotes the leading edge of the CME at its

central axis) due to the interaction between the CME and the streamer ahead of it. The

Wilcox Solar Observatory (WSO)source surface synoptic charts (R = 2.5 radial model)

(http://wso.stanford.edu/synsourcel.html) indicated that the location of the *current* sheet

(streamer belt neutral line) was $\sim$ S23° on Apr 2 - 3, 2010, *just ahead of the CME LE.*

*The streamer was marked by arrows in the COR1 and COR2 images (Figure 2).* The

CME/shock front was interacting with and indented by the streamer; an arc-like front

formed, as marked by thick arrows in Figure 5a and 5b. The heliocentric distances of the

shock along the Sun-Earth line and the LE on April 3, 20:09 UT are $\sim$ 56 $R_s$ and $\sim$ 49 $R_s$,

respectively. In Figure 5b, when the CME propagated farther out into the HI2-A FOV,

the shock sheath and the flux rope ejecta along the LE had been compressed together

and we can only see one complex compressed front. The ejecta along the Sun-Earth line

is too faint to see due to the further expansion.

Figure 6 (top panel) shows a time-distance $r(t)$ plot of the shock along the Sun-Earth

line with PA = 95°, where distances are derived from elongation angles in the J-map using

the three methods discussed above. We used the CME direction $\phi = 75°$ with respect to

STA (i.e., E8° with respect to Earth) for the Fixed-$\phi$ and Harmonic Mean approximations.

The direction was chosen so that $r(t)$ matched best with both the FR model fit results

and the observed SAT at Wind. The bottom panel of Figure 6 is the inferred velocity

of the shock. Here we omitted some distance points (6 points in this case) instead of

using adjacent data points to compute velocities to avoid large errors caused by distance

measurement errors. The velocity uncertainties are estimated assuming 1%, 2% and 3%

fractional errors in the distance measurements for COR2, HI1 and HI2, respectively, the

same as in *Wood et al.* [2010].

230    We found that the three approximations yield similar profiles within the COR2 and

231    HI1 FOV, but not in the HI2 FOV. The Point-P approximation produced a dramatic

232    deceleration, while the Fixed-$\phi$ approximation produced a large acceleration. These are

233    apparent accelerations and caused by *the apparent leading edges seen by HI. Due to a*

234    *projection effect and the CME angular width as it expands, the actual LE of the CME*

235    *is not seen by HI but the far-side or near-side flank of the CME,* resulting in artificial

236    distance increases and decreases (c.f. Figure 4 in *Wood et al.* [2010]). Among three

237    approximations, the Harmonic Mean method yields a more plausible kinematic profile.

238    Compared to the Wind SAT and in situ plasma bulk velocity in the sheath, marked by

239    red "X" symbols in Figure 6, the Harmonic Mean method gives the smallest errors of $\sim$

240    2 hours and $\sim$ 50 km/s respectively. Note that there is an overlap of distances from the

241    J-map and the flux rope model fit in COR2, denoted by orange plus symbols in the figure.

242    These two distances are shown to be consistent with each other.

## 3. Simulation with Numerical Heliospheric Model

243    To fully investigate the three-dimensional (3D) evolution and formation of the CME-

244    driven shock in the inner heliosphere, we used the WSA-Cone-ENLIL model. The WSA-

245    Cone-ENLIL model [e.g., *Odstrčil et al.*, 1996; *Odstrcil and Pizzo*, 1999; *Odstrcil et al.*,

246    2005] is well-known in the solar-helio community, and ENLIL version 2.3a is currently

247    available to users at the Community Coordinated Modeling Center (CCMC). ENLIL is a

248    time-dependent 3D MHD model of the heliosphere, and it solves for plasma mass, momen-

249    tum and energy density, as well as magnetic field, using a Total-Variation-Diminishing

250    Lax-Friedrich (TVDLF) algorithm [*Toth and Odstrcil*, 1996]. Its inner radial boundary

251    is located beyond the sonic point, typically at 21.5 $R_s$ (or 0.1 AU) for WSA (30 $R_s$ for

MAS), and the outer boundary is set at 2.0 AU. In the simulation spherical coordinates are used, and the three independent spatial variables are the radial position $r$, the meridional (latitude) angle $\theta$ , and the azimuthal (longitude) angle $\phi$. The meridional and azimuthal extents span 30°-150° and 0°-360°, respectively. The computational region has 512×60×180 grid points, and the uniform spacing of computational grid points are $\Delta r =$ 0.794 $R_s$, $\Delta\theta = 2°$, and $\Delta\phi = 2°$.

The CME is input into the ENLIL simulation domain as a hydrodynamic spherical cloud. This ejecta has a uniform velocity and diameter corresponding to the fitted radial CME speed and width. Parameters describing the CME's geometry and kinematics, such as size, speed and direction, can be obtained by fitting the cone model (or other forward-modeling techniques, e.g. flux rope model) to coronagraph observations [e.g., *Xie et al.*, 2004, 2009; *Krall and St.Cyr*, 2006; *Thernisien et al.*, 2006]. Further, the model assumes that the ejecta density has the density four times larger than the mean value in the fast stream and the same temperature as in the fast stream. It is assumed that the momentum flow and thermal pressure are constant at the inner boundary (0.1 AU) and that the density and temperature in the fast stream is 250 cm$^{-3}$ and 0.8 MK, respectively. The input values were chosen by matching the simulated properties of the shock upstream reasonable well with in situ *measurements* at 1AU.

The numerical simulation is done in two stages: 1) setup the background solar wind based on the Wang-Sheeley-Arge (WSA) [e.g., *Arge and Pizzo*, 2000; *Arge et al.*, 2004] or MAS [e.g., *Linker et al.*, 1999; *Riley et al.*, 2001] models; 2) insert a CME propagating in that background at the time when the observed CME passes the inner boundary (which is usually at 21.5 $R_s$ for WSA). In the simulation, we used the flux rope model fit results

<sup>275</sup> of actual speed (1011 km/s), face-on half angular width (37°), and direction (described in

<sup>276</sup> Section 2.2) as input parameters of the CME. The background solar wind was set up using

<sup>277</sup> the WSA model with photospheric magnetograms from the National Solar Observatory's

<sup>278</sup> (NSO) Global Oscillation Network Group (GONG) system, and the CME was launched

<sup>279</sup> into the computational heliospheric domain at the inner boundary 21.5 $R_s$ at t = 13:29

<sup>280</sup> UT.

## 4. Simulation Results

### 4.1. Comparison of the simulation results with in-situ observations

<sup>281</sup>   Figure 7 shows the simulated density in the ecliptic plane (left panel) and meridian plane

<sup>282</sup> (middle panel) as two-dimensional (2D) density contours on April 4 at 18:00 UT (movies

<sup>283</sup> are available online: http://ccmc.gsfc.nasa.gov/database_SH/h_xie_100311_SH_1.php *and*

<sup>284</sup> *in the online supplementary materials*). In the figure W (West) is up and E (East) is

<sup>285</sup> down in the ecliptic plane (left panel); and N (North) is up and S (South) is down in

<sup>286</sup> the meridian plane (middle panel). The Sun-Earth line is roughly horizontal with the

<sup>287</sup> Earth to the right. The heliographic location of the Earth is S6.3W00, i.e., in the center

<sup>288</sup> of the ecliptic plane and slightly southward in the meridian plane, as marked by yellow

<sup>289</sup> filled circles. The 2D density contours show that the CME has encountered two slow,

<sup>290</sup> dense streamers: one is located at the west flank of the CME and another is located at

<sup>291</sup> the center of the CME along the LE. The interaction between the CME and the dense

<sup>292</sup> streamers and the ambient solar wind has led to the formation of an arc-like structure at

<sup>293</sup> the CME LE (middle panel) and caused the IMF (black-white dashed line) to be deflected

<sup>294</sup> (left panel). The right panel of Figure 7 shows the simulated (blue solid lines) and the

<sup>295</sup> observed Wind solar wind plasma and magnetic field data (red dotted lines) at 1 AU

between April 2 and 9. The IP shock arrived at Wind on April 5 at 07:58 UT, followed by an ICME from April 5 at 12:00 UT to April 6 at 17:00 UT. Figure 8 is the in situ Wind observation data plus the Dst index. From Figure 8, we can see that the long-duration geomagnetic storm was first *caused* by a negative $B_y$ with a peak of $\sim$ -16 nT on Apr 5, 18:00 UT, and then enhanced farther by long-duration negative $B_z$ and $B_y$ of $\sim$ -7 nT. The observed ICME has a smooth magetic rotation and enhanced magnetic strength $|B|$, low proton temperature $T$ and plasam $\beta$, and a declining velocity $V$ profile (due to the ICME expansion in the solar wind). However, it cannot be fitted to any magnetic cloud models [c.f., *Möstl et al.*, 2010] because the ICME was southward directed (S25W03) and only its northern flank passed over Earth.

The ENLIL model predicted the shock arrival at Earth at 08:57 UT on April 5, with an error of $\sim$ 1.0 hour compared to the Wind SAT of 07:58 UT. Thus the ENLIL model provided a good prediction of the SAT for this event. Note that, however, the model requires the CME density and temperature as input at 0.1 AU which are not direct measurements, *thus adding a degree of uncertainty.* We have performed runs *by assuming that the CME has the density* either four times or twice larger than the fast stream value, and it yields a variation in SAT (shock arrival time) of $\sim$ 7 hrs. Furthermore, since the ENLIL ejecta is a pure hydrodynamic structure, the absence of the CME internal magnetic structure has caused the model to overestimate plasma density $N$ and temperature $T$, and to underestimate total $B$ field of the ICME.

## 4.2. Comparison of the simulation results with J-maps

In order to study the evolution of the IP shock driven by the CME, we need to find the locations of the shock front where the sudden increase of density (or velocity) occurs.

318   Figure 9 (left panels) shows an example of how to locate the simulated shock, where we

319   plot density times the square of radial distance $nr^2$ as function of distance $r$: a) along the

320   LE propagation direction; b) along the Sun-Earth line on April 5 at 06:01 UT. In Figures

321   9a and b, locations of the shock front, upstream and downstream are marked by three

322   vertical lines $r_{sk}$, $r_{up}$, and $r_{dw}$. We define a shock front $r_{sk}$ by locating the largest slope of

323   $nr^2$, i.e. largest $d(nr^2)/dr$. The shock downstream is defined as $r_{dw} = r_{sk}$-2 spacing grids

324   *because* the average thickness of the shock is $\sim 4$ spacing grids due to the limitation of

325   the 3D code resolution. We choose the shock upstream $r_{up}$ to be $r_{sk}$+5 spacing grids to

326   ensure that the selected upstream has fallen into the smooth ambient solar wind region,

327   where $nr_{up}^2$ remains nearly constant.

328   Right panels of Figure 9 plot the upstream density $nr_{up}^2$, the downstream density $nr_{dw}^2$,

329   and the shock compression ratio $nr_{dw}^2/nr_{up}^2$ as function of time : c) along the LE propaga-

330   tion direction and d) along the Sun-Earth line. Comparing Figures 9c and d, we can see

331   that the shock compression ratios along two propagation directions have similar trends.

332   Both curves experience an initial increase and then gradually decrease. The compression

333   ratio along the LE (Sun-Earth) propagation direction reaches a maximum value of 5.81

334   (6.10) on April 4, 06:03 UT. The background solar wind density, $nr_{up}^2$, remains nearly con-

335   stant along the Sun-Earth line and slightly increases along the LE propagation direction

336   , due to the slow dense streamer ahead of the CME. The mean values of the solar wind

337   density along the LE and Sun-Earth are 6.64 cm$^{-3}$ and 4.16 cm$^{-3}$, respectively. We apply

338   these values to the kmTII method in Section 5. Note that the maximum compression

339   ratios along the both LE and Sun-Earth propagation directions are greater than the the-

340   oretical threshold of 4 [Priest, 1982]. This is due to a limitation of the 3D code resolution

producing the shock front thickness to be too large (the spacing of grids) [*Steinolfson et al.*, 1975].

Figure 10a compares the simulated time-distance profiles of the shock along the LE and Sun-Earth line with the time-distance profiles from J-maps along the LE and Sun-Earth line. All the distances in the figure are measured for the shock front. We found that the shock propagation along the LE propagation direction lagged behind the one along the Sun-Earth line in both the ENLIL model and J-map, due to the interaction between the CME and the streamer at the LE. HI2-A movies (see online supplementary materials in the HTML) clearly show that the shock front has been flattened and compressed and the Earthward shock front (a faint brightness enhancement) arrived earlier at 1 AU than the shock front along the LE.

The shock arrival times along the LE and Sun-Earth line are 12:10 UT and 08:57 UT in the ENLIL model; and 17:27 UT and 05:42 UT in the J-map (all these times refer to April 5). The linear-fit shock velocities along the LE and Sun-Earth line are 778 km/s and 849 km/s in the ENLIL model; and 712 km/s and 925 km/s in the J-map. The differences in SAT between the ENLIL model and J-map are $\sim$ 5 hours along the LE, and $\sim$ -3 hours along the Sun-Earth line. The differences in linear shock speed between the ENLIL model and J-map are 66 km/s along the LE, and $\sim$ -76 km/s along the Sun-Earth line. Thus the simulation results agree with the observations within the error range of the measurements. The simulation reproduced the overall dynamics of the shock propagation with realistic large scale structures.

Note that the difference between the two propagation directions for the shock, in the ENLIL model, is much smaller than that in the J-map. The differences in SAT and shock

364 speed in the ENLIL model are ∼ 3 hours and 71 km/s between the two directions; and

365 11.5 hours and 213 km/s in the J-map. We will discuss this in Section 6.

366    Figure 10b shows the time-velocity profiles of the CME inferred from the distances in

367 Figure 10a. All four velocity profiles show small decelerations. The linear-fit decelerations

368 along the Sun-Earth line are similar, with values of -0.49 and -0.50 m/s$^2$ in the ENLIL

369 model and J-map, respectively. But the linear-fit deceleration in the ENLIL model is

370 smaller (-0.82 m/s$^2$) than that (-1.43 m/s$^2$) in the J-map along the LE. The deceleration

371 from the J-map along the LE is consistent with the IP acceleration $a = 2.193 - 0.0054u$

372 from *Gopalswamy et al.* [2005b]'s empirical shock arrival (ESA) model, where $u$ is the

373 CME speed. For $u = 712$ km/s; $a = -1.65$ m/s$^2$. The ESA model gives an SAT of 15:30

374 UT for an earthward speed of 925 km/s, which gives an error of ∼ 7.5 hours.

## 5. The "kmTII" Technique

375    For the April 3, 2010 CME, no decameter-hectometric (DH) type II radio burst was

376 detected. But a kilometric type II (kmTII) radio burst starting from April 4 00:58 to 16:33

377 UT was detected by Wind/WAVES. Such events are generally rare and have a relatively

378 slower average speed compared to other CMEs with radio-loud shocks as discussed in

379 *Gopalswamy et al.* [2010]. Figure 11 shows the dynamic spectrum of the kmTII radio

380 burst recorded by the TNR receiver on April 4, 2010. Note the scale of the vertical axis

381 is in units of 1/f. The solid line represents the linear fit of the drifting 1/f as a function of

382 time. Using a simple density model in which $n = n_0/r^2$ ($n_0$ is the plasma density at 1 AU

383 in units of cm$^{-3}$) [e.g., *Leblanc et al.*, 1998], the time-distance profile of the CME-driven

384 shock can then be obtained from the frequency drift given by $r(t) = a\sqrt{n_0}/f(t)$, where

385 $r(t)$ is the heliocentric distance where the kmTII occurs in units of AU, $f(t)$ is the drifting

frequency in units of kHz, and $a = 9$ or $18$ is a constant for fundamental or harmonic

emission respectively. The derived shock speed is $V_{sh} = a\sqrt{n_0} \times \frac{d}{dt}(1/f) \times 1.5 \times 10^8$ (km/

s) [*Reiner et al.*, 1998]. Figure 12 plots the time-distance profile of the shock propagation

inferred from the kmTII method, superimposed with trajectories extracted from the J-

maps. Open circles represent data points extracted from the J-maps along the LE (blue)

and the Sun-Earth line (red), and green diamonds represent the results derived from the

kmTII method using the ENLIL model density a) at Earth $n_0 = 4.16$ cm$^{-3}$ and b) at the

LE $n_0 = 6.64$ cm$^{-3}$ in Figure 9. In Figure 12a, assuming that the kmTII occurs near the

Sun-Earth line, the kmTII estimated linear shock speed is 656 km/s and the estimated

SAT is 22:57 UT, yielding errors of $\sim$ 15 hours and 269 km/s, compared to the Wind

SAT of 07:58 UT and the J-map Earthward shock speed of 925 km/s. In Figure 12b,

the kmTII is assumed to occur near the shock at the LE. The kmTII prediction gives a

linear-fit shock speed of 829 km/s and the predicted SAT is 09:44 UT, yielding errors of $\sim$

2 hours and 96 km/s, compared to the Wind SAT and the J-map Earthward shock speed.

Thus applying the plasma density value near the LE has improved the kmTII prediction

error from 15 hours to 2 hours, and the kmTII prediction accuracy largely relies on the

value of the plasma density it used. Table 1 summarizes the derived shock propagation

characteristics from the ENLIL simulation, J-maps, and kmTII method.

## 6. Discussion and Conclusion

We have comprehensively investigated the evolution and propagation of the April 3, 2010

CME-driven shock, combining STEREO and SOHO white light observations, kilometric

type II radio data with the simulation using the WSA-Cone-ENLIL model. We used the

KS06 flux rope model fit to SECCHI and LASCO observations to determine the CME

speed, size and direction, as well as its time-distance profile when the CME is within the C3 FOV. We derived the time-distance profile of the CME/shock in the heliosphere from the J-maps constructed from SECCHI images, from near the Sun all the way to 1 AU. The shock front was seen clearly in the HI1-A images staring from April 3 $\sim$ 15:29 UT. Three methods, i.e., P-Point, Fixed-$\phi$, and Harmonic Mean, were used to derive the radial distances from elongation angles in the J-maps. The obtained results show that the harmonic mean approximation gives the best results for the time-distance and time-velocity profiles of the shock, yielding the smallest errors compared to the Wind observations of the shock arrival time and in situ plasma bulk velocity in the sheath. To fully investigate the formation and evolution of the shock and predict the shock arrival time, we used the WSA-Cone-ENLIL model simulation and the kmTII technique. The kinematic analysis from J-maps together with in-situ data provided us with a valuable opportunity to validate the simulated results and the kmTII prediction.

We found that the ENLIL model provided good predictions on the shock arrival time along both the Sun-Earth line and the CME-LE propagation directions. The ENLIL model predicted the SAT at Earth on April 5 at 08:57 UT and the SAT at 1AU along the LE of $\sim$ 12:10 UT with $\sim$ *1 ± 7 hours and* $\sim$ *5 ± 7 hours* errors, respectively, compared to the Wind SAT and J-map SAT along the LE. It also reproduced the overall dynamics of the shock propagation with realistic large scale structures in the simulation, including the background solar wind density along the Sun-Earth line, the locations of streamer outflows, the CME-streamer interaction, and the flattened arc-like shock front along the LE.

₄₃₀      The kmTII prediction largely relies on the coronal density model and the electron

₄₃₁ density $n_0$ at 1 AU, which is assumed to be the average solar wind value 7.2 cm$^{-3}$ in

₄₃₂ *Cremades et al.* [2007]. To investigate the possibility of using the ENLIL model density

₄₃₃ to improve the kmTII prediction, we applied the solar wind density obtained from the

₄₃₄ simulation to the kmTII method. With $n_0 = 4.16$ cm $^{-3}$ at Earth and $n_0 = 6.64$ cm $^{-3}$ at

₄₃₅ the LE, the estimated shock speeds are 656 km/s and 829 km/s, yielding SATs of 22:57

₄₃₆ UT and 09:44 UT and errors of $\sim 15$ hours and $\sim 2$ hours, compared to the Wind SAT

₄₃₇ of 07:58 UT.

₄₃₈      Note that, however, the good prediction of $\sim 2$ hours was due to the cancellation of

₄₃₉ two errors, i.e., the error in the location where the kmTII occurred and the density error

₄₄₀ from the simulation. First, the kmTII radio emission was assumed to occur at the CME

₄₄₁ LE, where the shock had been intensified due to the CME-streamer interaction and low

₄₄₂ Alfvén speed (high density) in the streamer, as shown in Figure 9a. Second, the actual

₄₄₃ error is $\sim 7.7$ hours when compared to the J-map SAT of 17:27 UT at the LE, indicating

₄₄₄ the ENLIL model had overestimated the density along the LE, resulting in a smaller SAT,

₄₄₅ which yielded a small error of $\sim 2$ hours (compared with 07:58 UT).

₄₄₆      One possible reason for the ENLIL model's overestimating the plasma density along

₄₄₇ the LE may be because the simulation didn't reproduce the small flux-rope like V-shaped

₄₄₈ structure which is observed by HI-A. On closer examination of HI-A image movie, we

₄₄₉ see that a small flux-rope like V-shaped structure was formed out of the streamer outflow

₄₅₀ ahead of the CME LE. The first appearance time of this small FR-like V-shaped structure

₄₅₁ in HI1-A was around April 3 20:09 UT. Its formation was likely due to reconnection of

₄₅₂ magnetic field lines at the tip of helmet streamers [e.g., *Rouillard et al.*, 2010]. This V-

shaped structure was observed to be entrained by the streamer outflows and traveling with the similar speed as the solar wind. The CME caught up with the V-shaped structure at ~ 02:09 UT on April 4, as shown in HI2-A image movie, and then merged together around ~ 20:09 UT. An arc-like shaped front was formed due to the large compression caused by the interaction of the CMEs in the HI2-A movie. This interacting duration was consistent with the time period when the kilometer type II burst occurred, suggesting that the CME-streamer (or CME-CME) interaction enhanced the shock intensity and produced the type II radio burst [e.g., *Gopalswamy et al.*, 2001]. Since the ENLIL model didn't include the CME's internal magnetic field, it didn't reproduce the V-shaped FR-like structure formed out of the streamer. This may explain why the simulation results didn't reproduce as big of a difference of the shock along two propagation directions, i.e., the LE and the Sun-Earth line, as that shown in the J-map. It may also explain why the ENLIL model produced too large of a plasma density upstream of the shock in order to compensate the magnetic field pressure from the small FR-like CME along the LE. If a CME-driven shock occurs in a background solar wind which is more homogeneous, using the ENLIL model has the potential to improve the kmTII prediction. In turn, the kmTII observations can constrain and help improve the future modeling of shocks.

## References

482 Arge, C. N., and V. J. Pizzo (2000), Improvement in the prediction of solar wind conditions

483     using near-real time solar magnetic field updates, *J. Geophys. Res.*, *105*, 10,465–10,480.

484 Arge, C. N., J. G. Luhmann, D. Odstrcil, C. J. Schrijver, and Y. Li (2004), Stream

485     structure and coronal sources of the solar wind during the may 12th, 1997 cme, *J.

486     Atmos. Sol. Terr. Phys.*, *66*, 1295–1309.

487 Bougeret, J.-L., et al. (1995), Waves: The Radio and Plasma Wave Investigation on the

488     Wind Spacecraft, *Space  Sci. Rev.*, *71*, 231–263, doi:10.1007/BF00751331.

489 Bougeret, J. L., et al. (2008), S/WAVES: The Radio and Plasma Wave Investigation on

490     the STEREO Mission, *Space  Sci. Rev.*, *136*, 487–528, doi:10.1007/s11214-007-9298-8.

491 Brueckner, G. E., et al. (1995), The Large Angle Spectroscopic Coronagraph (LASCO),

492     *Solar Phys.*, *162*, 357–402, doi:10.1007/BF00733434.

493 Cremades, H., O. St.Cyr, and M. Kaiser (2007), A tool to improve space weather forecasts:

494     Kilometric radio emissions from Wind/WAVES, *Space  Weather*, *5*, S08,001.

495 Eyles, C. J., et al. (2009), The Heliospheric Imagers Onboard the STEREO Mission, *Solar

496     Phys.*, *254*, 387–445, doi:10.1007/s11207-008-9299-0.

Gopalswamy, N., S. Yashiro, M. L. Kaiser, R. A. Howard, and J.-L. Bougeret (2001), Radio Signatures of Coronal Mass Ejection Interaction: Coronal Mass Ejection Cannibalism?, *Astrophys. J. Lett.*, *548*, L91–L94, doi:10.1086/318939.

Gopalswamy, N., E. Aguilar-Rodriguez, S. Yashiro, S. Nunes, M. L. Kaiser, and R. A. Howard (2005a), Type II radio bursts and energetic solar eruptions, *Journal of Geophysical Research (Space Physics)*, *110*, A12S07, doi:10.1029/2005JA011158.

Gopalswamy, N., A. Lara, P. K. Manoharan, and R. A. Howard (2005b), An empirical model to predict the 1-AU arrival of interplanetary shocks, *Advances in Space Research*, *36*, 2289–2294, doi:10.1016/j.asr.2004.07.014.

Gopalswamy, N., H. Xie, P. Mäkelä, S. Akiyama, S. Yashiro, M. L. Kaiser, R. A. Howard, and J.-L. Bougeret (2010), Interplanetary Shocks Lacking Type II Radio Bursts, *Astrophys. J.*, *710*, 1111–1126, doi:10.1088/0004-637X/710/2/1111.

Howard, T. A., D. F. Webb, S. J. Tappin, D. R. Mizuno, and J. C. Johnston (2006), Tracking halo coronal mass ejections from 0-1 AU and space weather forecasting using the Solar Mass Ejection Imager (SMEI), *Journal of Geophysical Research (Space Physics)*, *111*, A04105, doi:10.1029/2005JA011349.

Kahler, S. W., and D. F. Webb (2007), V arc interplanetary coronal mass ejections observed with the Solar Mass Ejection Imager, *J. Geophys. Res.*, *112*, 9103, doi:10.1029/2007JA012,358.

Kaiser, M. L., T. A. Kucera, J. M. Davila, O. C. S. Cyr, M. Guhathakurta, and E. Christian (2008), The STEREO Mission: An Introduction, *Space Sci. Rev.*, *136*, 5–16.

Krall, J., and O. C. St.Cyr (2006), Flux-Rope Coronal Mass Ejection Geometry and Its Relation to Observed Morphology, *Astrophys. J.*, *652*, 1740–1746, doi:10.1086/508337.

Leblanc, Y., G. A. Dulk, and J.-L. Bougeret (1998), Tracing the electron density from the corona to 1 AU, *Solar Phys.*, *183*, 165–180.

Linker, J., et al. (1999), Magnetohydrodynamic modeling of the solar corona during whole sun month, *J. Geophys. Res.*, *104*, 9809–9830.

Lugaz, N., A. Vourlidas, and I. I. Roussev (2009), Deriving the radial distances of wide coronal mass ejections from elongation measurements in the heliosphere ̌2013 application to CME-CME interaction, *Annales  Geophysicae*, *27*, 3479–3488.

Möstl, C., M. Temmer, T. Rollett, C. J. Farrugia, Y. Liu, A. M. Veronig, M. Leitner, A. B. Galvin, and H. K. Biernat (2010), Stereo and wind observations of a fast icme flank triggering a prolonged geomagnetic storm on 5-7 april 2010, *Geophys. Res. Lett.*, *37*, L24,103, doi:10.1029/2010GL045,175.

Odstrcil, D., and V. Pizzo (1999), Three-dimensional propagation of CMEs in a structured solar wind flow: 1. CME launched within the streamer belt, *J. Geophys. Res.*, *104*, 483–492.

Odstrcil, D., V. Pizzo, and C. N. Arge (2005), Propagationof the 12 May 1997 interplanetary coronal mass ejection in evolving solar wind structures, *J. Geophys. Res.*, *110*, A02,106, doi:10.1029/2004JA010,745.

Odstrčil, D., M. Dryer, and Z. Smith (1996), Propagation of an interplanetary shock along the heliospheric plasma sheet, *J. Geophys. Res.*, *101*, 19,973–19,986, doi: 10.1029/96JA00479.

Priest, E. R. (1982), *Solar magneto-hydrodynamics*, Dordrecht, Holland ; Boston : D. Reidel Pub. Co. ; Hingham, 74P

Reiner, M. J., M. L. Kaiser, J. Fainberg, and R. G. Stone (1998), A new method for studying remote type II radio emissions from coronal mass ejection-driven shocks, *J. Geophys. Res.*, *103*, 29,651–29,664.

Riley, P., J. A. Linker, and Z. Mikic (2001), An empirically-driven global MHD model of the solar corona and inner heliosphere, *J. Geophys. Res.*, *106*, 15,889– 15,901.

Rouillard, A. P., et al. (2010), Intermittent release of transients in the slow solar wind: 1.Remote sensing observations, *J. Geophys. Res.*, *115*, A04,103, doi:10.1029/2009JA014,471.

Rouillard, A. P., et al. (2011), Interpreting the Properties of Solar Energetic Particle Events by Using Combined Imaging and Modeling of Interplanetary Shocks, *Astrophys. J.*, *735*, 7, doi:10.1088/0004-637X/735/1/7.

Sheeley, N. R., J. H. Walters, Y.-M. Wang, and R. A. Howard (1999), Continuous tracking of coronal outflows: Two kinds of coronal mass ejections, *J. Geophys. Res.*, *104*, 24,739– 24,768, doi:10.1029/1999JA900308.

Sheeley, N. R., Jr., et al. (2008), Heliospheric Images of the Solar Wind at Earth, *Astrophys. J.*, *675*, 853–862, doi:10.1086/526422.

Steinolfson, R. S., M. Dryer, and Y. Nakagawa (1975), Numerical MHD simulation of interplanetary shock pairs, *J. Geophys. Res.*, *80*, 1223–1231, doi:10.1029/JA080i010p01223.

Thernisien, A. F. R., R. A. Howard, and A.Vourlidas (2006), Modeling of Flux Rope Coronal Mass Ejections, *Astrophys. J.*, *652*, 763–773.

Toth, G., and D. Odstrcil (1996), Comparison of some flux corrected transport and total variation diminishing numerical schemes for hydrodynamic and magnetohydrodynamic problems, *J. Comput. Phys.*, *128*, 82–100.

Wood, B. E., R. A. Howard, and D. G. Socker (2010), Reconstructing the Morphology of

an Evolving Coronal Mass Ejection, *Astrophys. J.*, *715*, 1524–1532.

Wood, B. E., C.-C.Wu, R. A. Howard, D. G. Socker, and A. P. Rouillard (2011), Empirical

Reconstruction and Numerical Modeling of the First Geoeffective Coronal Mass Ejection

of Solar Cycle 24, *Astrophys. J.*, *729*, 70.

Xie, H., L. Ofman, and G. Lawrence (2004), Cone model for halo CMEs: Application to

space weather forecasting, *J. Geophys. Res.*, *109*, A03,109, doi:10.1029/2003JA010,226.

Xie, H., O. C. S. Cyr, N. Gopalswamy, S. Yashiro, J. Krall, M. Kramar, and J. Davila

(2009), On the Origin, 3D Structure and Dynamic Evolution of CMEs Near Solar Min-

imum, *Solar Phys.*, *259*, 143–161.
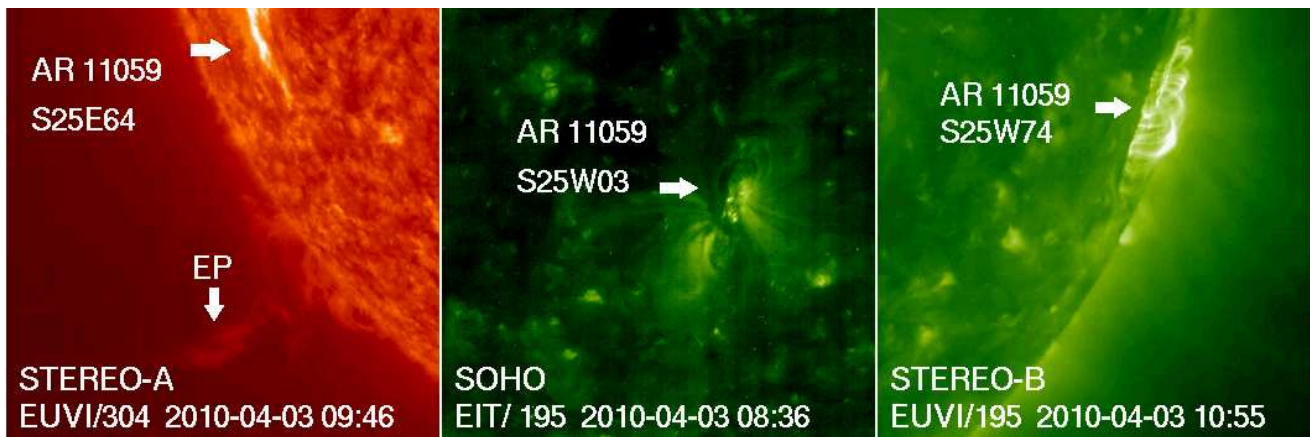
**Figure 1.**    (Left) EUVI 304 $\mathring{A}$ image on STEREO A showing an eruptive prominence to the south of AR 11059 at 09:46 UT; (middle) EIT 195 $\mathring{A}$ image at 08:36 UT and (right) EUVI 195 $\mathring{A}$ image at 10:55 UT showing a sigmoid to post eruption arcade flare in AR 11059 observed from SOHO and STEREO B, respectively.
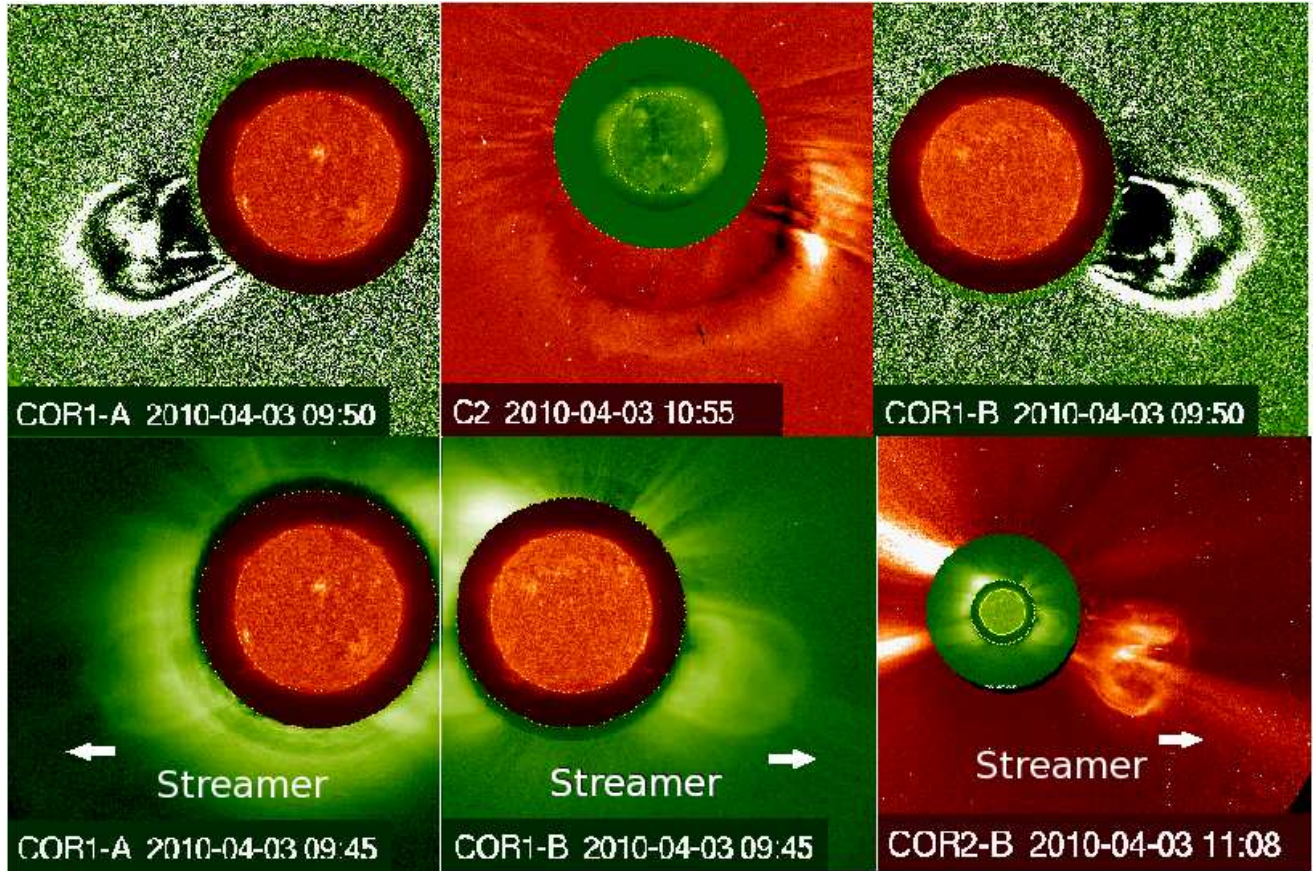
**Figure 2.** (Top) STEREO A (left) and B (right) COR1 running-difference images superimposed with EUVI 304 $\mathring{A}$ image at 09:50 UT and SOHO C2 running-difference image (middle) superimposed with EIT 195 $\mathring{A}$ image at 10:55 UT showing edge-on and face-on views of the *April 03 CME*. (Bottom) STEREO A (left) and B (middle) COR1 original images superimposed with EUVI 304 $\mathring{A}$ image at 09:45 UT and STEREO B COR2 image (right) at 11:08 UT showing a streamer located ahead of the CME leading edge.
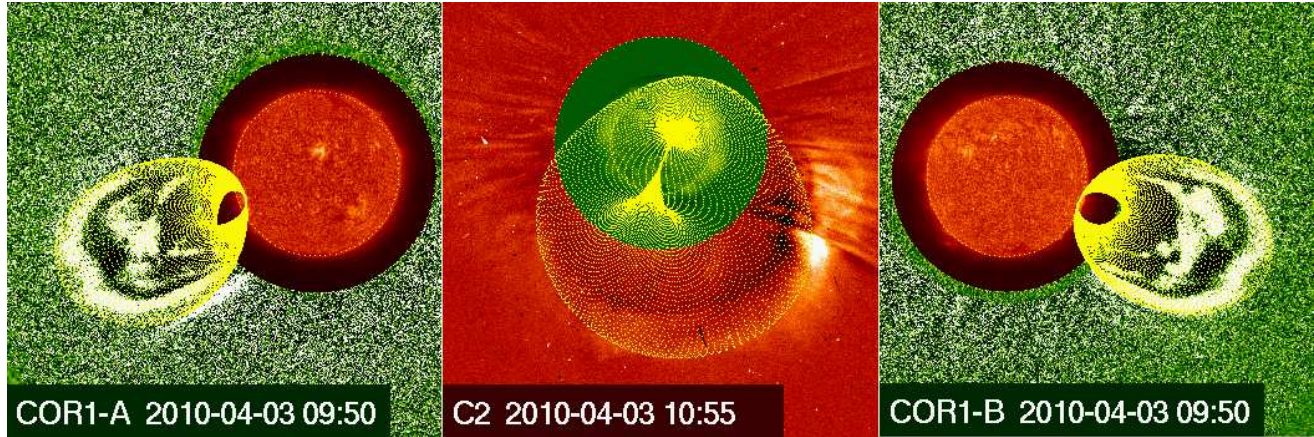
**Figure 3.**   Flux-rope Modeling of the Apr 3, 2010 CME. STEREO A and B COR1 and SOHO C2 images with the flux-rope projected wireframe (yellow curves) overlaid on top.
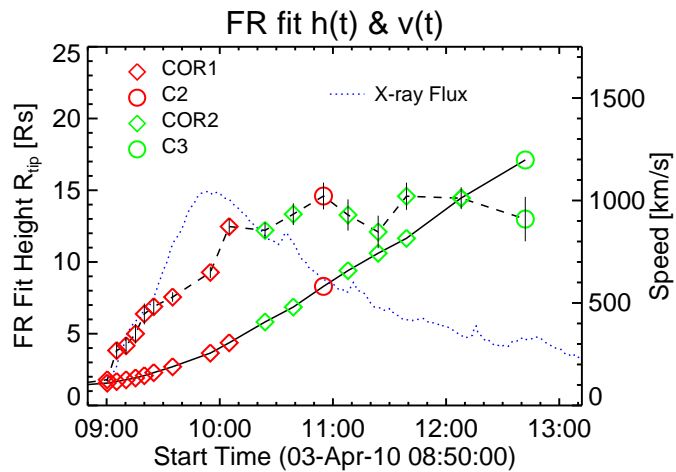


**Figure 4.**     The flux-rope model fit results to the CME in COR1 (red diamonds), COR2 (green diamonds), C2 (red open circle), and C3 (green open circle) images. The model fit height-time profile and derived velocity profile are denoted by the solid and dashed lines respectively, overplotted with the GOES X-ray flux (blue dotted line).The short vertical lines in the figure indicate the velocity uncertainties.
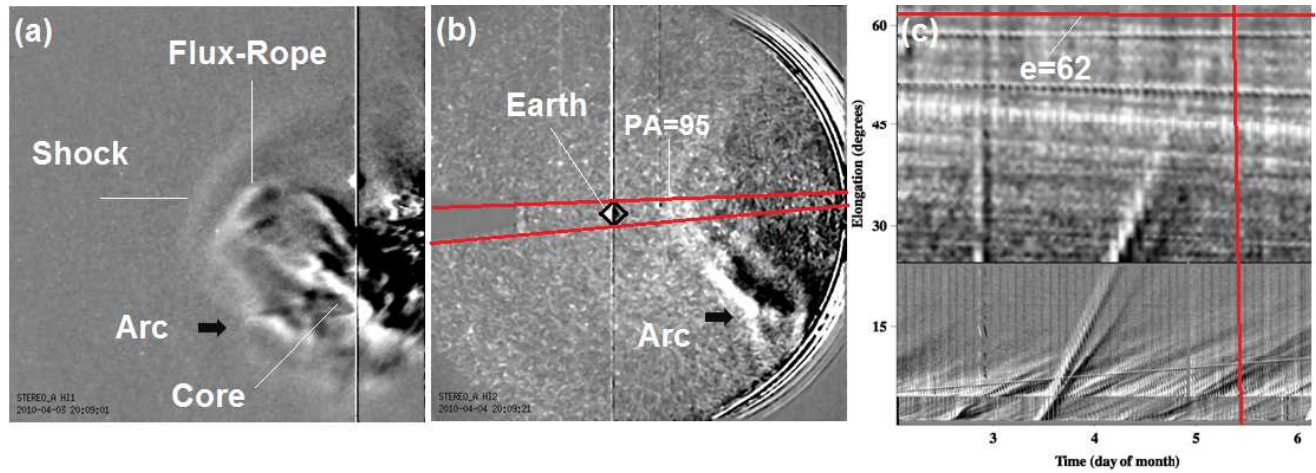
**Figure 5.** From left to right: running difference image of HI1-A on April 3, 20:09 UT, HI2-A image on April 4, 20:09 UT and a time-elongation J-map along PA = 95°. Shock front, CME features and the Earth location are marked in the HI images. Thick arrows in (a) and (b) denote the CME arc-like leading edge which has been indented. Two red lines in (b) label the slit we use to make the Jmap at PA = 95°. The horizontal and vertical lines in the J-map mark the Earth position (at 62°) and the time (05:42 UT) when the shock arrived at Earth.
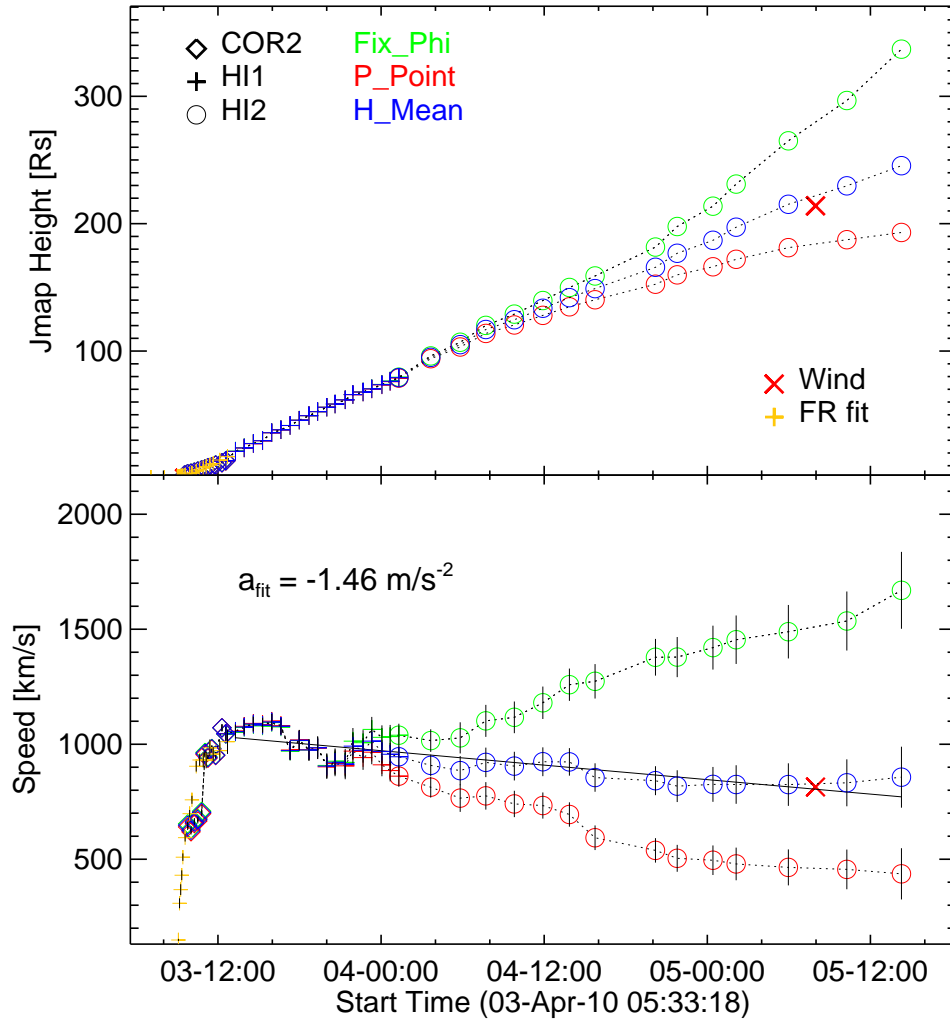
**Figure 6.** (Top) time-distance and (bottom) time-velocity profiles along the Sun-Earth line, for the three approximations denoted by red, green, and blue respectively. The Fixed-$\phi$ method produces an apparent acceleration in HI2 FOV, while the Point-P method produces an apparent deceleration. The Harmonic Mean method yields the most plausible kinematic profile, with the smallest errors compared to the Wind observations.
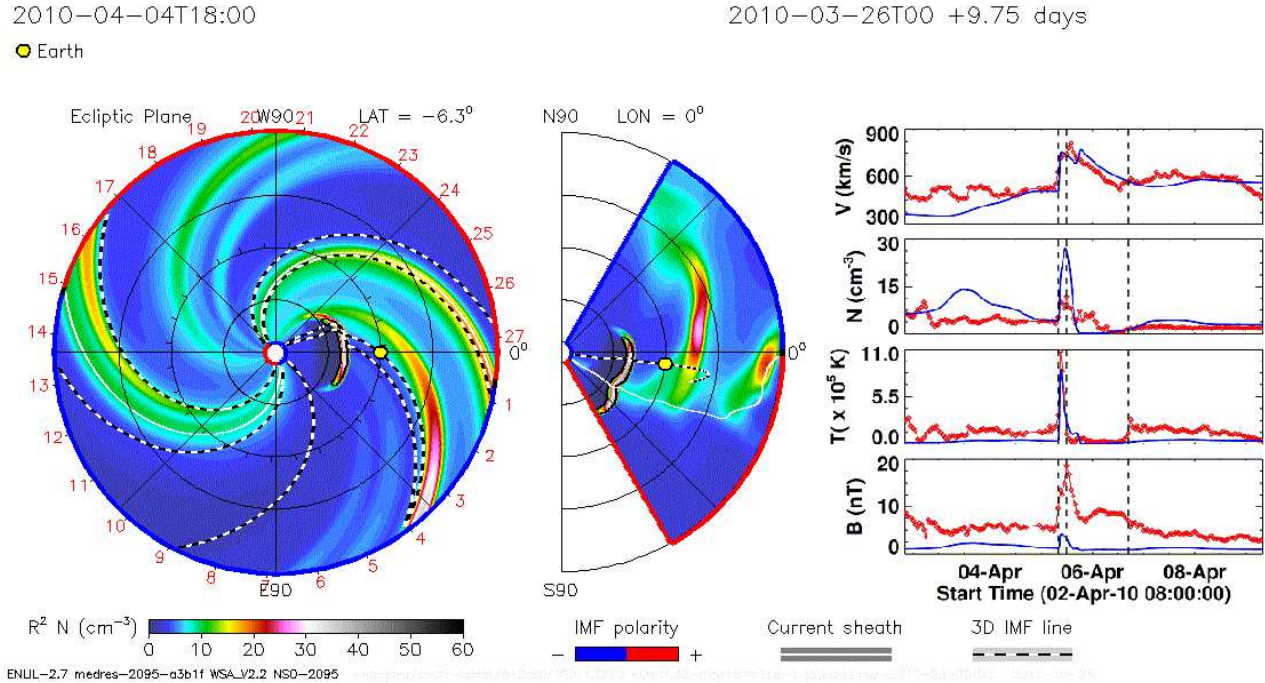
**Figure 7.**    Simulation results of 2D density contours in the ecliptic plane (left panel) and meridian plane (middle panel) on April 4, 18:00 UT. The density in the simulation is normalized for an $r^{-2}$ falloff with distance. Right panel is the comparison of the simulated (blue solid lines) and observed Wind solar wind plasma and magnetic field data (red dotted lines) at 1 AU between April 2 and 9.
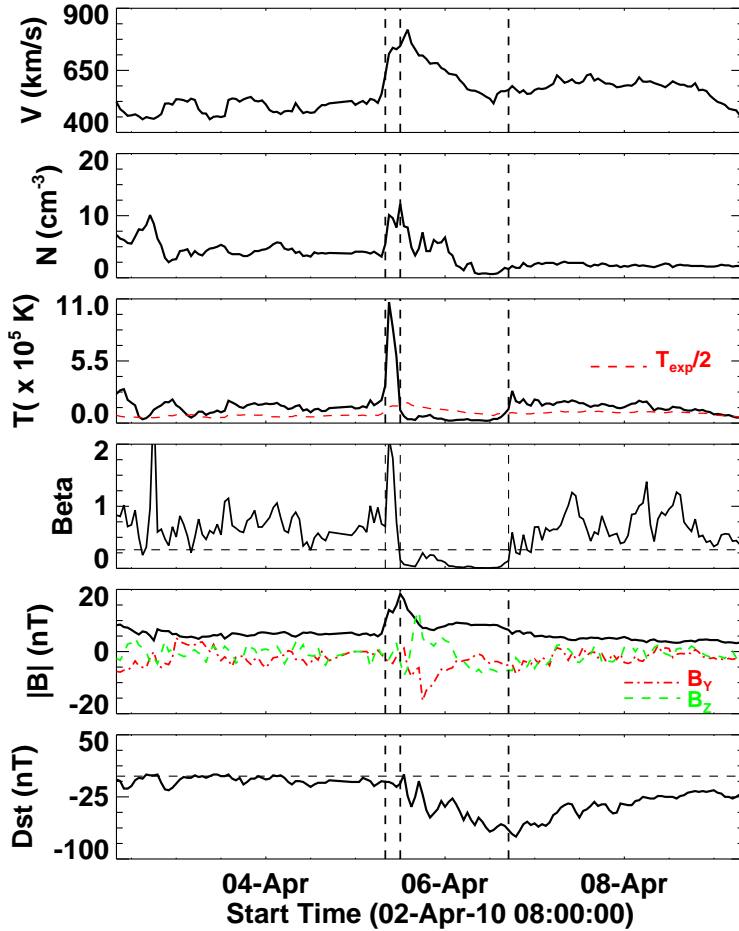
**Figure 8.**     Solar wind plasma and magnetic field data (Wind). From top to bottom: proton bulk velocity $V$, proton number density $N$, proton temperature $T$, plasma $\beta$, magnetic field magnitude $|B|$ and components $B_y$ and $B_z$, and Dst index. The three vertical dashed lines indicate the shock arrival and the ICME interval, where the ICME is identified by the interval that shows proton temperature depression below half the expected solar wind temperature $T_{exp}$. The horizontal lines in $\beta$ and $D_{st}$ are lines for $\beta = 0.3$ and $D_{st} = 0$ , *respectively.*
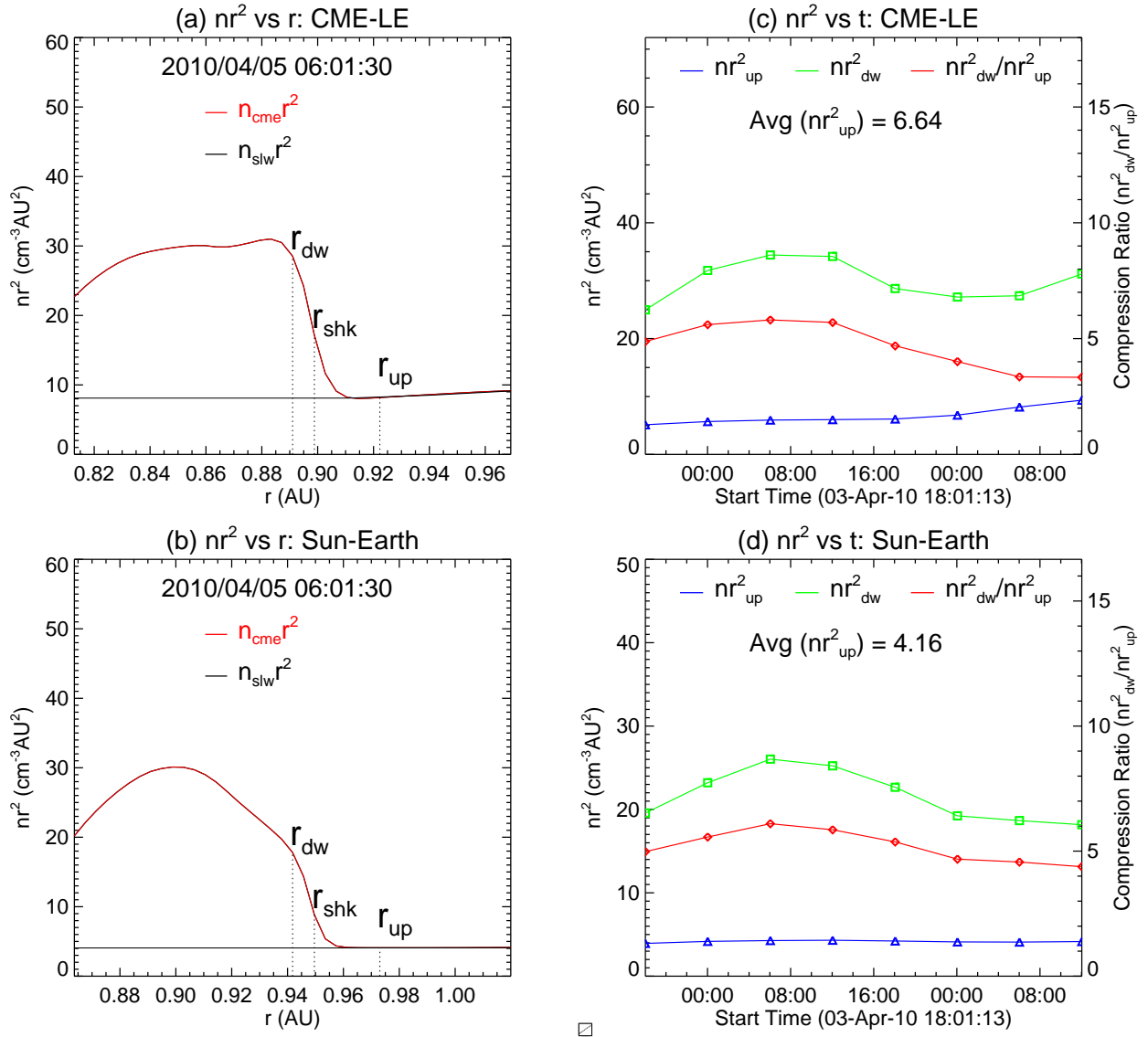
**Figure 9.** (Left) Simulation results of $nr^2$ (density times square of radial distance) as function of distance $r$: a) along the LE propagation direction; b) along the Sun- Earth line on April 5, 06:01:30 UT, where red and black lines denote the CME and ambient solar wind plasma density respectively, and three dashed vertical lines mark locations of the shock front, upstream and downstream. (Right) $nr^2_{up}$, $nr^2_{dw}$, shock compresson ratio $nr^2_{dw}/nr^2_{up}$ as function of time : c) along the LE and d) along the Sun-Earth line.
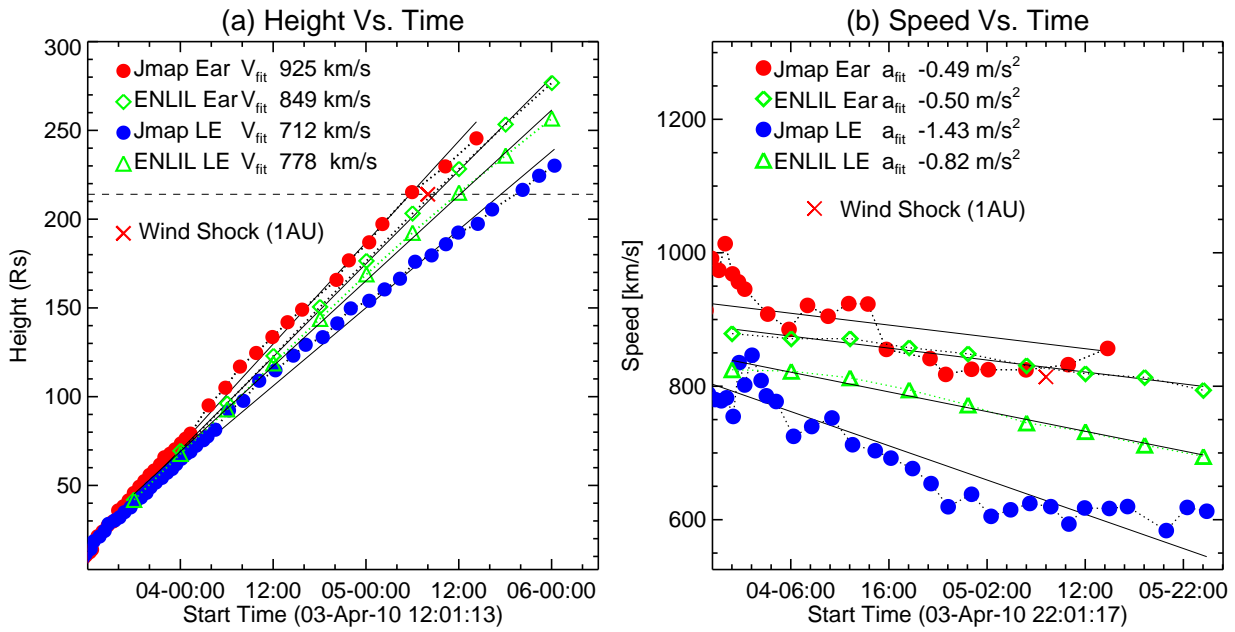
**Figure 10.**    Comparison of (a) time-distance and (b) time-velocity profiles of the shock from the ENLIL model and J-maps, where $V_{fit}$ and $a_{fit}$ are the linear-fit velocity and acceleration.
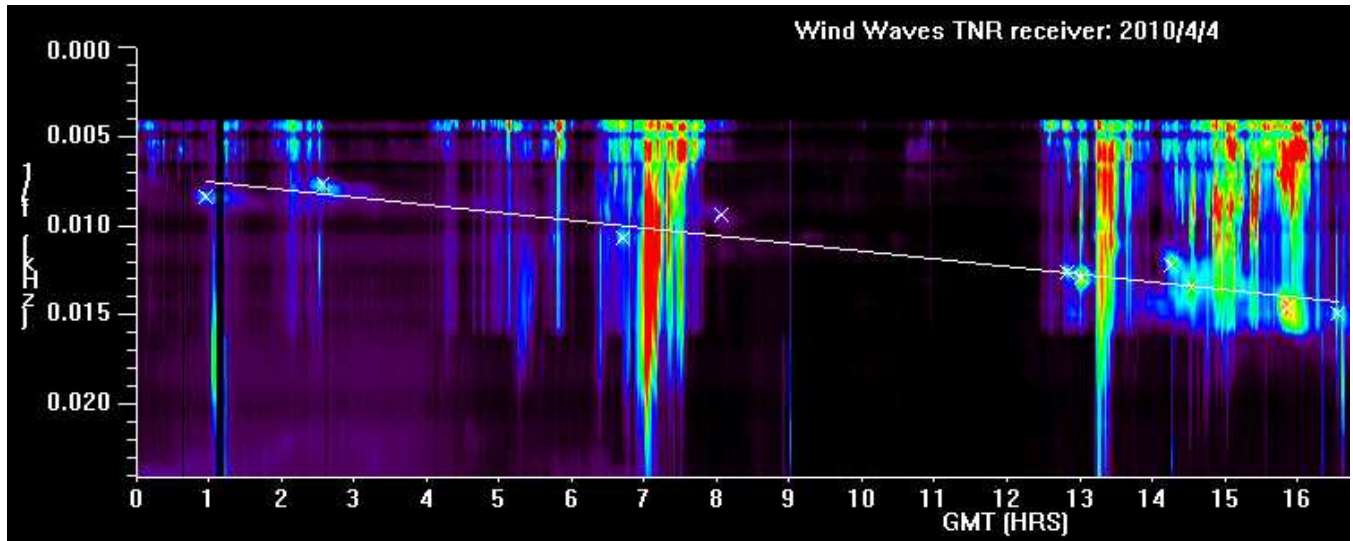


**Figure 11.**    kmTII dynamic spectrum detected by the TNR receiver on April 4 2010. Note the scale of the vertical axis is in units of 1/f. "X" symbols in the figure mark the selected data points in the spectrum.
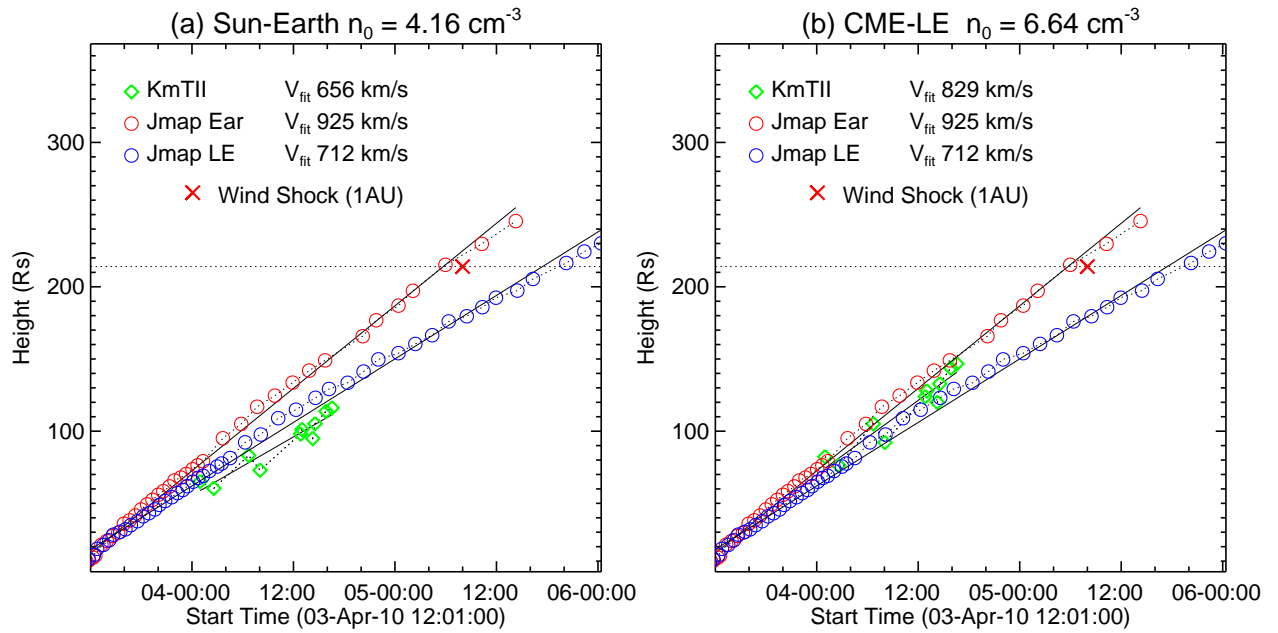
**Figure 12.** Comparison of the time-distance profiles of the shock from J-maps and kmTII with a) $n_0 = 4.16$ cm$^{-3}$ along the Sun-Earth line and b) $n_0 = 6.64$ cm$^{-3}$ along the CME LE.

**Table 1.**   Summary of the predicted shock properties from the simulation, J-maps and kmTII

method.

| | ENLIL | | J-map | | kmTII | |
|---|---|---|---|---|---|---|
| | Sun-Earth | CME-LE | Sun-Earth | CME-LE | Sun-Earth | CME-LE |
| | | | | | $n_0(4.16)$ | $n_0(6.64)$ |
| | | | | | $(\mathrm{cm}^{-3})$ | $(\mathrm{cm}^{-3})$ |
| SAT (UT) [a] | 08:57 | 12:10 | 05:42 | 17:27 | 22:57 | 09:44 |
| $V_{fit}$ (km s$^{-1}$) [b] | 849 | 778 | 925 | 712 | 656 | 829 |
| $a_{fit}$ (m s$^{-2}$) [c] | -0.50 | -0.82 | -0.49 | -1.43 | — | — |

[a]  Shock arrival time; all times are on Apr 5

[b]  Shock linear-fit velocity

[b]  Shock linear-fit acceleration